Transport signatures of fragile glass dynamics in the melting of the two-dimensional vortex lattice

I. Maccari [1,*,†] Bal K. Pokharel [2,3,*,‡] J. Terzic [2,4] Surajit Dutta,[5] J. Jesudasan,[5] Pratap Raychaudhuri,[5] J. Lorenzana [6]
C. De Michele [7] C. Castellani [7,6] L. Benfatto [7,6,§] and Dragana Popović [2,3,¶]

[1]*Department of Physics, Stockholm University, 106 91 Stockholm, Sweden*
[2]*National High Magnetic Field Laboratory, Florida State University, Tallahassee, Florida 32310, USA*
[3]*Department of Physics, Florida State University, Tallahassee, Florida 32306, USA*
[4]*Department of Physics and Astronomy, Western Kentucky University, Bowling Green, Kentucky 42101, USA*
[5]*Tata Institute of Fundamental Research, Homi Bhabha Rd, Colaba, Mumbai 400005, India*
[6]*Institute for Complex Systems (ISC-CNR), UOS Sapienza, P.le A. Moro 5, 00185 Rome, Italy*
[7]*Department of Physics, Sapienza University of Rome, P.le A. Moro 2, 00185 Rome, Italy*

In a two-dimensional superconducting vortex lattice, the melting from the solid to the isotropic liquid can occur via an intermediate phase that retains orientational correlations. The effect of such correlations on transport and their interplay with the quenched disorder remain open questions. We perform magnetotransport measurements in a wide range of temperatures and magnetic fields on a weakly pinned two-dimensional vortex system in amorphous MoGe films. While at high fields, where quenched disorder dominates, we recover the typical strong-glass behavior of a vortex liquid, at low fields the resistivity shows a clear crossover to a fragile vortex glass. Our findings, supported by numerical simulations, suggest that this is a signature of heterogeneous dynamics that arises from the presence of orientational correlations.

I. INTRODUCTION

Thermal melting of two-dimensional (2D) crystalline solids has been investigated in a variety of systems, including colloids, electrons on the surface of liquid helium, rare-gas atoms on substrates such as graphite, liquid-crystal films, dust plasmas, and vortices in thin superconducting (SC) films in a transverse magnetic field [1,2]. The melting transition is generally understood to be driven by the proliferation of topological defects, as described by the Berezinskii-Kosterlitz-Thouless-Halperin-Nelson-Young (BKTHNY) theory [3–5]. According to BKTHNY, for weak enough quenched disorder the transition from the 2D (weakly pinned) solid to the isotropic liquid phase occurs via an intermediate phase called hexatic. In the hexatic phase, free dislocations appear, breaking the quasi-long-range positional order, but preserving the hexagonal orientational one. By increasing the temperature (T) further, free disclinations form and a fully isotropic liquid is established. This melting sequence has indeed been

detected by scanning-tunneling-spectroscopy (STS) imaging of vortices in 2D superconductors [6–9], but the morphology of dislocations can be affected by microscopic details, resulting in the apparent coexistence of isotropic with hexatic liquid as well as with smecticlike (striped) regions [6], or the emergence of chains of dislocations [10]. The presence of competing orders may give rise to metastable states and the associated slow dynamics in many systems [11]. An STS study on amorphous MoGe (*a*-MoGe) thin films did observe [9] a strong suppression of the vortex diffusivity in the presence of hexatic correlations compared to the isotropic liquid. However, the nature of the vortex dynamics near the melting transition, its effect on electrical transport, and its evolution with magnetic field (H) have not been explored in relatively clean *a*-MoGe samples, where finite orientational correlations may arise even in the liquid phase.

We perform extensive magnetotransport measurements on *a*-MoGe thin films similar to those used in the STS studies that revealed the presence of hexatic correlations at low H [8,9]. Our key experimental finding is that, for fixed low fields $H < 9$ T, the low-T resistivity follows a Vogel-Fulcher-Tamman (VFT) law, i.e. $\rho(T) = \rho_{\mathrm{VFT}}$, where

$$\rho_{\mathrm{VFT}} = \tilde{Z} \exp\left(-\frac{\tilde{W}(H)}{T - \tilde{T}_0(H)}\right). \quad (1)$$

Here $\tilde{W}(H)$ is a constant independent of T, and $\tilde{T}_0(H)$ marks the temperature at which the linear resistivity vanishes. As H increases, we find that $\tilde{T}_0(H)$ is suppressed to zero, i.e., standard Arrhenius behavior is recovered, and nonlinear voltage-current characteristics V-I emerge. The VFT

*These authors contributed equally to this work.

†ilaria.maccari@fysik.su.se

‡bkp16@fsu.edu

§lara.benfatto@roma1.infi.it

¶dragana@magnet.fsu.edu

law [12–14] generally describes the behavior of the so-called fragile liquids above the glass transition, and it is usually attributed to the emergence of dynamical heterogeneities [15]. We argue that the VFT law at low H results from dynamical heterogeneities due to emergent orientational correlations as the melting transition is approached. This is supported by our Monte Carlo simulations of the 2D XY model in the presence of a transverse H. We show that the orientational order leads to a caging effect that suppresses vortex diffusivity, which follows a VFT law as one enters the hexatic phase, i.e., the vortex diffusion coefficient

$$D_v = Z \exp\left(-\frac{W(H)}{T - T_0(H)}\right). \qquad (2)$$

The temperature T_0 identifies the liquid-solid transition temperature corresponding to the vanishing of the superfluid density. Our results thus reveal a fragile glass-like dynamics associated with the thermal melting of a weakly pinned 2D vortex lattice, and a crossover to a strong-glass ($\tilde{T}_0 = T_0 = 0$) behavior at higher H, resulting from the interplay of orientational correlations and disorder.

II. RESULTS

Our samples are 22-nm-thick a-MoGe films with SC transition temperature $T_c \sim 7.6$ K at zero field (see Appendix A), and low normal-state sheet resistances $R_s \approx 78$ Ω indicative of a very weak disorder [9,16]. Here T_c is defined as the temperature at which the linear resistance $R \equiv \lim_{I \to 0} V/I$ (i.e., ρ) falls below the experimental noise floor (see Appendix A). The characteristic lengthscales for vortex distortions parallel to the applied H and caused by thermal fluctuations or pinning are of the order of several μm [17,18], i.e., much larger than the sample thickness t. Therefore, the vortex lattice (VL) in these films is indeed 2D, although the SC state is 3D ($t > \xi$, where $\xi \sim 5$ nm is the SC coherence length [17]). In the field range of interest, any geometric, edge barrier effects on the vortex motion are negligible [19].

Measurements of $\rho(H)$ at fixed T (Fig. 4 in Appendix B) were performed with heavily filtered wiring (see Appendix B) due to the extreme sensitivity of the SC state to external radiation [9]. The $\rho(H)$ data were used to determine $T_c(H)$ (i.e., the corresponding field H_c for a given T) and the upper critical field $H_{c2}(T)$, which we define as the magnetic field where $\rho = 0.95 \rho_N$ at a given T ($\rho_N = 0.17$ mΩ cm is the normal-state resistivity). Since $T_c(H)$ depends on the experimental resolution, it does not necessarily allow one to determine the real boundary between the liquid and solid phase, nor the possible transition to an orientational liquid phase.

To explore the melting of the VL, we extract $\rho(T)$ curves at fixed H [Fig. 1(a); see also Fig. 5(a)]. A rapid, orders-of-magnitude change of ρ with T, observed for fields below about 12 T and with no sign of saturation at low T, suggests an exponential $\rho(T)$ dependence. Indeed, the Arrhenius law,

$$\rho_{\mathrm{Arrh}} = \rho_0 \exp\left(-\frac{U(H)}{T}\right), \qquad (3)$$

is often used to describe the linear resistivity in the vortex liquid regime at low enough T [20]. In this picture of a thermally assisted flux flow (TAFF), vortices move collectively
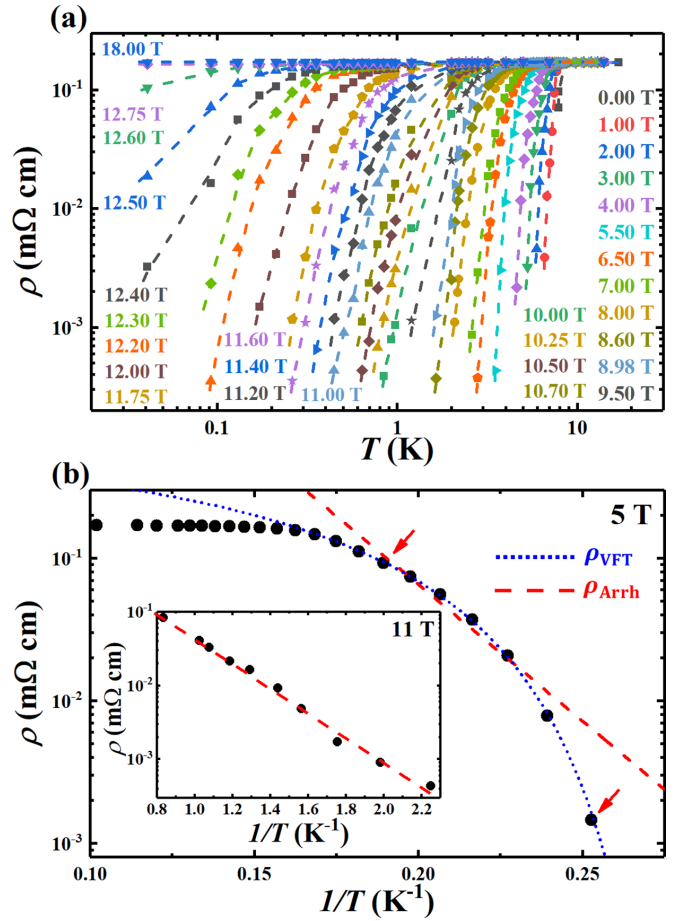

FIG. 1. (a) $\rho(T)$ at selected H, extracted from the data in Fig. 4 for sample 1. The dashed lines guide the eye. (b) $\rho(T)$ fitted with the Arrhenius (red dashed line) and VFT (blue dotted line) laws for $H = 5$ T; the fits are performed for the data points within the two red arrows, although the VFT describes the data also at higher T. Here $\tilde{T}_0 = (3.42 \pm 0.01)$ K [the fit to Eq. (2) gives $T_0 = (3.37 \pm 0.01)$ K]. Inset: The data for $H = 11$ T are well described by ρ_{Arrh} (or ρ_{VFT} with $\tilde{T}_0 \approx 0$ K), as shown by the red dashed line. The excitation current $I_{\mathrm{exc}} = 100$ nA for $H = 5$ T and $I_{\mathrm{exc}} = 10$ nA for $H = 11$ T.

and overcome pinning barriers via thermal excitations when $T \lesssim U(H)$. Although ρ is nonzero, V-I remains non-Ohmic (i.e., nonlinear) for $I \neq 0$ [23]. We note that Eq. (3) assumes ρ is finite at all nonzero T. However, when the superfluid phase sets in, which corresponds to a solid phase for the VL, ρ vanishes, so deviations from (3) should be observed whenever the critical temperature is finite and the transition is not strongly first-order (i.e., in the absence of a large, abrupt jump).

We have performed fits of the $\rho(T)$ data, for fixed H, according to ρ_{Arrh}. Two examples are shown in Fig. 1(b), one for a low field ($H = 5$ T) and another for a high field ($H = 11$ T). While at high H the Arrhenius fit works extremely well down to T_c, at low fields we systematically find significant deviations (see also Fig. 6 in Appendix C), with a faster suppression of ρ than predicted by ρ_{Arrh}. Interestingly, such deviation can be captured very well by the VFT law, Eq. (1). Since we are interested in the vortex diffusivity, we have also performed fits to $\rho(T) = (h/2e)^2 n_v D_v/(k_B T)$, where $n_v = B/\Phi_0$ is the
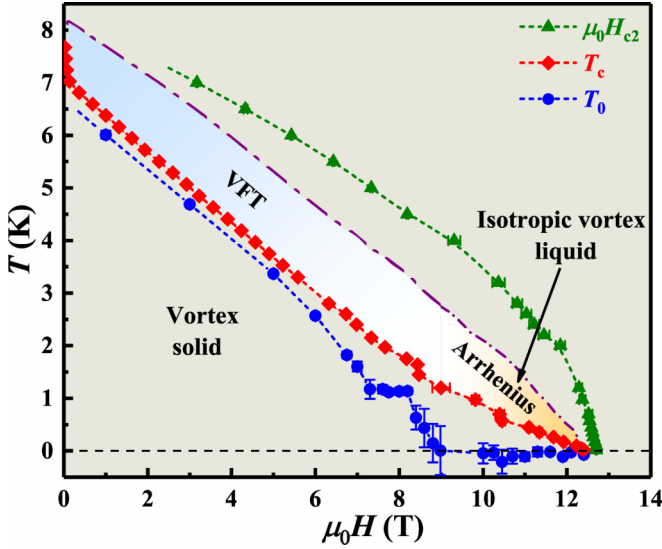
FIG. 2. (T, H) phase diagram (sample 1). $T_0(H)$ (blue dots) are obtained from the VFT fits, whose range of validity is marked by the shaded blue "VFT" region; the error bars reflect the standard errors of the fits and $T_0 = \tilde{T}_0$. For $H \gtrsim 9$ T, ρ can only be fitted with the Arrhenius law in the shaded orange "Arrhenius" region. Here the isotropic vortex liquid freezes into an amorphous vortex glass at $T = 0$. The purple dot-dashed line shows the high-T extent of the VFT and Arrhenius fits. Green triangles: the upper critical field $H_{c2}(T)$; here ρ reaches 95% of its normal-state value. Red diamonds: $T_c(H)$, where ρ drops below the experimental noise floor. Error bars in $T_c(H)$ and H_{c2} are the uncertainty in defining the magnetic field corresponding to each quantity within our experimental resolution.

vortex density ($\Phi_0 = h/2e$ is the quantum of magnetic flux attached to a single vortex, h is Planck's constant, and e is electron charge), k_B is the Boltzmann constant, and D_v is given by Eq. (2). For both (1) and (2), the fitting parameters were extracted using global minimization, and were typically found to be the same within error [see, e.g., Figs. 1(b) and 6]; in particular, $T_0 = \tilde{T}_0$. The parameters $\tilde{Z}$ and Z are the same within the proportionality constant between ρ and D_v, consistent with the exponential term dominating $\rho(T)$. Hence, hereafter we present only the VFT fitting parameters obtained using Eq. (2).

Figure 2 shows $T_0(H)$, $T_c(H)$, $H_{c2}(T)$ [see also Fig. 5(b) in Appendix B], and the range of T where the VFT and the Arrhenius fits are effective (see Fig. 7 in Appendix C for all the fitting parameters as a function of H). We find that for fields below $H^* \simeq 9$ T the VFT fit gives a significantly better description of the data. With increasing H, however, T_0 decreases gradually, and vanishes near $H^* \simeq 9$ T. For $9 \lesssim H \lesssim 12.5$ T, $T_0(H) = 0$ within experimental error and, indeed, $\rho(T)$ curves are well described by the Arrhenius fits, consistent with $T_0 = 0$ (see Fig. 8). In this regime, we find that $U(H) = U_0 \ln(H_0/H)$ (see Fig. 9 in Appendix C), as expected from the TAFF model and the logarithmic vortex-vortex interactions in 2D [20]. The behavior observed in the high-field ($H > H^*$, "Arrhenius" in Fig. 2 with $T_0 = 0$, $T > T_c$) regime is, therefore, consistent with the thermally activated collective motion of vortices in the presence of strong pinning, similar to previous studies of disordered SC films, including a-MoGe

[21,22]. This conclusion is further supported by our measurements of the differential resistance (dV/dI) versus dc current bias I_{dc} at fixed H (see Appendix D for a detailed discussion). In particular, the non-Ohmic (nonlinear) V-I characteristic observed for $I_{dc} \neq 0$ at low enough T [Figs. 10(a) and 10(b) in Appendix D] is expected from the motion of vortices in the presence of disorder, i.e., it is a signature of a viscous vortex liquid [23]. As T increases, nonlinear behavior is no longer observed [Figs. 10(c) and 10(d) in Appendix D]. As $T < T_c$, where ρ drops below our noise floor, a finite I_{dc} is then needed to depin a measurable number of vortices [Fig. 10(e) in Appendix D]. Our transport results thus suggest that in this regime, an isotropic vortex liquid freezes into an amorphous vortex glass as $T \to 0$, i.e., the solid phase is only realized at $T = 0$.

In the normal state ($H > H_{c2}$), V-I characteristics are Ohmic [Figs. 10(b) and 10(e) in Appendix D], as expected. In the low-field ($H < H^*$, $T_0 \neq 0$, $T > T_c$) regime ("VFT" in Fig. 2), we also find Ohmic behavior [Fig. 10(f) in Appendix D]. The key question is the origin of the observed VFT behavior.

Within the context of glasses, one can define a temperature T_0, where the relaxation time diverges and the configurational entropy vanishes [15]. T_0 is below the temperature T_g where the dynamical glass transition occurs, the value of which depends on the sensitivity of the probe. The VFT fit allows one to overcome such an experimental upper bound and to infer T_0, that is, the temperature scale at which the residual entropy is comparable to that of the ordered state. In our experiment, the role of T_g is then played by T_c, where the resistance drops below the measurable threshold, while T_0 corresponds to the transition to the truly superfluid phase where D_v (or ρ) vanishes. In that case, we expect that the "VFT" region above T_c shows the extent of the dynamically heterogeneous vortex liquid in the (T, H) phase diagram (Fig. 2). Analogies to glasses were used to propose the VFT law (1) to describe the slowing down and freezing of the strongly disordered 3D vortex matter [24,25], but in our a-MoGe films the disorder-dominated high-field regime ($T_0 = 0$) is described, in contrast, by the TAFF model (3). Thus our results strongly suggest that quenched disorder is not the main origin of the VFT suppression of the vortex diffusivity observed at lower H.

III. MONTE CARLO SIMULATIONS

To explore the possibility that the presence of orientational correlations may give rise to dynamical heterogeneities and the VFT behavior, we performed Monte Carlo (MC) simulations on the 2D XY model in a transverse field. Its Hamiltonian reads

$$H_{XY} = -J \sum_{i, \mu = \hat{x}, \hat{y}} \cos\left(\theta_i - \theta_{i+\mu} + F_i^\mu\right), \qquad (4)$$

where θ_i represents the SC phase of the condensate, J is the effective Josephson-like interaction between nearest-neighboring sites, and $F_i^\mu = \frac{2\pi}{\Phi_0} \int_{r_i}^{r_{i+\mu}} A_i^\mu dr_\mu$ is the Peierls phase resulting from the minimal substitution prescription. The intensity of the magnetic field $B\hat{z} = \vec{\nabla} \times \vec{A}$ can be expressed in terms of the quantum-flux fraction f passing through a unitary plaquette $f = Ba^2/\Phi_0$, where $a = 1$ is the
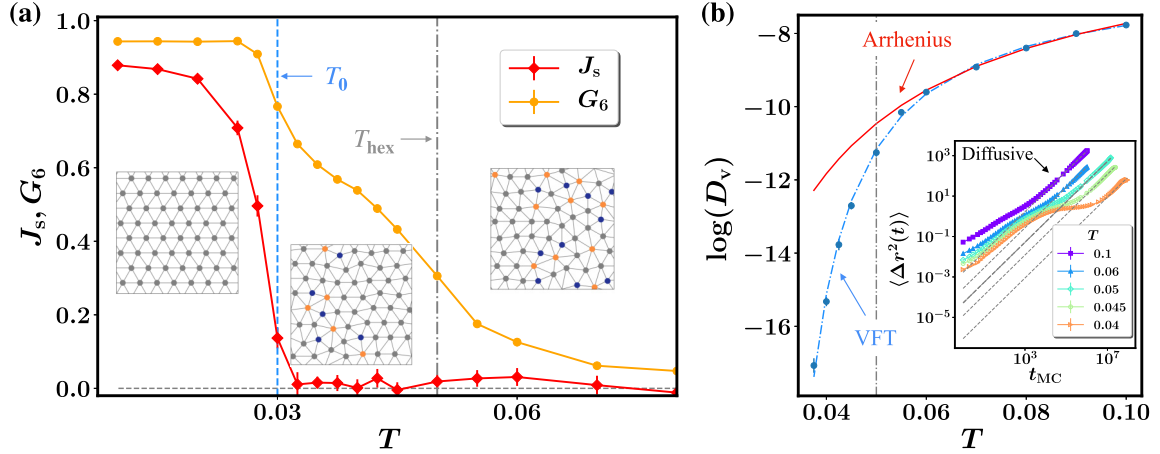
FIG. 3. (a) MC results of the T-dependence of the superfluid stiffness J_s and the G_6 orientational order parameter. The insets show snapshots of the VL at temperatures $T = 0.02, 0.04, 0.07$ from left to right, respectively. Blue dashed line: the temperature T_0 where the VFT fit of D_v shown in panel (b) vanishes. Gray dot-dashed line: the isotropic to the hexatic liquid transition temperature T_{hex} obtained from χ_6 (see Fig. 11 in Appendix E). Below $T \simeq T_0$, a pinned solid exists, with true quasi-long-range positional and long-range orientational order, as identified by a finite J_s and $G_6 \simeq 1$. Above T_0, the quasi-long-range positional order is lost due to the appearance of dislocations, formed by bound pairs of disclinations with opposite sign (marked with blue and orange dots in the VL snapshots). As T further increases above T_{hex}, isolated disclinations appear, leading to a fully isotropic liquid with vanishing orientational order. (b) T-dependence of the vortex diffusion constant D_v, extracted from the diffusive regime of the mean-square displacement shown in the inset. The dashed lines in the inset mark the linear fits $\langle \Delta r^2(t) \rangle \sim D_v t$ at selected T. In the main figure, the dashed blue line is a fit of D_v with the VFT law (2), while the continuous red line is the Arrhenius fit $D_{v,\text{Arrh}} = D_v^0 \exp(-U_v/T)$. The vertical gray dot-dashed line indicates T_{hex}.

lattice spacing. Within the model (4), vortices are topological excitations of the phase variable θ_i, allowing for the direct characterization [26–31] of the static properties of the solid-to-liquid transition, via computation of the phase rigidity. Dynamical effects, however, have been mainly studied via effective models where vortices are mapped into individual particles [10,32–34]. Here we show how model (4) allows us to address both aspects. Indeed, the solid phase can be identified via the superfluid response, and the dynamical properties of vortices can be characterized by tracking the diffusion of each individual vortex in time at a given T.

To establish the superfluid phase, we computed the superfluid stiffness J_s, namely the global phase rigidity of the condensate (see Appendix E). At the same time, to establish the orientational order of the VL, we computed the sixfold orientational order parameter G_6 (see Appendix E). The T dependence of J_s and G_6 is shown in Fig. 3(a), along with prototypical images of the corresponding VL; T is expressed in units of J/k_B. We can identify three distinct phases: a low-T SC phase, where the VL is a pinned solid with a complete hexagonal order ($G_6 \simeq 1$); a disordered non-SC phase at high T, where the VL has melted into an isotropic liquid ($G_6 \simeq 0$); and an intermediate phase, which is a liquid ($J_s = 0$) but with a persistent orientational order of the VL ($G_6 \neq 0$) (see also Fig. 12 in Appendix E). The isotropic to hexatic liquid critical temperature T_{hex} in Fig. 3 has been identified from the orientational susceptibility χ_6 (see Fig. 11 in Appendix E).

Our study of vortex dynamics reveals all the typical fingerprints of the hexatic phase, as identified in 2D soft-colloid systems [35–39]. We tracked in time each individual vortex, and we computed the vortex mean-square displacement $\langle \Delta r^2(t) \rangle$, where $\langle \cdots \rangle$ denotes the thermal average and the average over 10 independent numerical simulations, at several T

[see Fig. 13(b) in Appendix E and inset of Fig. 3(b)]. At high T, we find $\langle \Delta r^2(t) \rangle$ directly crosses over from a short-time subdiffusive regime to the typical long-time diffusive regime, where $\langle \Delta r^2(t) \rangle \sim D_v t$, with D_v the vortex diffusion constant. However, at the verge of the isotropic- to hexatic-liquid transition, an additional subdiffusive regime appears with a strong suppression of $\langle \Delta r^2(t) \rangle$ at intermediate timescales. This hallmark of dynamical heterogeneities is due to the caging mechanism provided by the finite orientational order in the hexatic phase (see also Video S1 of the Supplemental Material [40], described in Appendix G). The signatures of the dynamical heterogeneities persist at longer timescales, with a marked reduction at these temperatures of the asymptotic diffusion coefficient, defined as $D_v = \frac{1}{4} \lim_{t \to \infty} \langle \Delta r^2(t) \rangle / t$.

The resulting T-dependence of $D_v(T)$ is shown in Fig. 3(b). It is clear that Arrhenius law strongly deviates from the data at low T, and the VFT law provides a good description of the data, similar to our experimental findings in the lower-field regime. Also, we see an internal consistency between the static characterization and the vortex dynamics in the description of the transition from solid to liquid, i.e., T_0 extracted from the VFT fit almost coincides with the T where J_s vanishes [see Fig. 3(a)].

IV. DISCUSSION AND CONCLUSIONS

Our study has revealed similarities between the thermal melting of a 2D VL in weakly pinned a-MoGe films and the behavior of fragile glass-forming liquids. The results of our numerical work strongly support the existence in our samples of heterogeneous dynamics whose origin can be mainly attributed to the presence of orientational correlations, while

below T_0 a true superfluid state is recovered, in contrast to early conclusions [41].

Using the analogy with strong and fragile glasses [15], we can argue that the decrease of T_0 with increasing H signals a crossover from a fragile to a strong glass (with $T_0 = 0$). This is consistent with the magnetic field increasing the effective disorder [23], which suppresses the orientational correlations leading to a disordered state where the dynamics is no longer heterogeneous and the Arrhenius trend is recovered. The extrapolation of $T_0(H)$ to zero at $H^* \simeq 9$ T also suggests the existence of a quantum critical point separating the dissipationless solid (for $H < H^*$) from the SC vortex glass phase that only exists at $T = 0$. A similar field-tuned transition between two SC ground states with different ordering of the vortex matter, a vortex solid at lower H and a $T = 0$ vortex glass at higher H, has been observed also in underdoped copper-oxide high-T_c superconductors [42,43], which are relatively clean quasi-2D systems. In this context, it is interesting to speculate whether the low-temperature part of the $T_0(H)$ line corresponds to the so-called order-disorder transition that has been observed in numerous experiments on various SC materials [44].

Our work establishes an additional paradigm for the 2D vortex dynamics in the presence of weak quenched disorder, in close analogy with fragile glass dynamics of the 2D melting in soft-matter systems. Further insight into the physical mechanisms responsible for such heterogeneous dynamics of the melting of a 2D VL could come from experiments on more disordered thin films and theoretical exploration of its evolution in the presence of finite disorder. Moreover, thin films of other relatively clean amorphous SC materials could be tested with similar transport measurements to verify the general character of the resulting phase diagram. Other probes, such as scanning tunneling spectroscopy at various temperature and magnetic field ranges, could provide a more detailed understanding of such transitions. At the same time, our work establishes the 2D weakly pinned vortex lattice systems as an alternative platform to systematically investigate the fragile-to-strong glass crossover with the significant advantage of a single tuning parameter, the magnetic field H. This is a remarkable result since typically the well-known Angell plot is realized comparing different materials, each one being either a fragile or a strong glass. Our findings offer a fresh perspective on the universal emergence of glassy behavior in different research areas, ranging from SC vortex physics to soft-matter colloidal systems and physisorbed atom layers [45].

APPENDIX A: SAMPLES

a-MoGe films with thickness $t = 22$ nm were grown on surface-oxidized Si substrate through pulsed laser deposition. The reported chemical stoichiometry of these thin films, as seen from the dispersive x-ray analysis, is $Mo_{71\pm1.5}Ge_{29\pm1.5}$; their properties have been described in detail elsewhere [8,9,17]. The films were capped with a 2-nm-thick Si layer to prevent surface oxidation, and patterned in Hall bar geometry using a shadow mask. Detailed measurements were performed on two samples with dimensions 0.36 mm (width)×2.8 mm (length), and 1.1 mm distance between the voltage contacts. The two samples exhibited an almost identical behavior. For sample 1, the voltage contact width is 0.05 mm and the zero-field $T_c = (7.70 \pm 0.05)$ K; for sample 2, the voltage contact width is 0.025 mm and $T_c = (7.50 \pm 0.05)$ K. T_c is defined as the temperature at which the resistivity starts to rise above the experimental noise floor ($\sim3.6 \times 10^{-4}$ mΩ cm or ~0.5 Ω in resistance). Gold leads (≈50 μm in diameter) were attached to the samples (on top of a Si layer) using two-component EPO-TEK-E4110 epoxy. The resulting contact resistances were ~200 Ω each at room temperature.

APPENDIX B: MEASUREMENTS

Resistance was measured using the standard four-probe ac technique (~13 or 17 Hz) with either SR 7265 lock-in amplifiers or an LS 372 resistance bridge. Some of the measurements were performed using a dc reversal method with a Keithley 6221 current source and a Keithley 2182A nanovoltmeter. The excitation current densities were 0.1–4 A cm^{-2}, depending on the temperature, and low enough to avoid Joule heating. Specifically, a current of $I_{exc} = 10$ nA (density ~0.1 A cm^{-2}) was used for measurements at $T < 1$ K, while most of the $T > 1$ K measurements were done with 100 nA (density ~1 A cm^{-2}), making sure that the data are still in the Ohmic regime (i.e., that the V-I response at low currents is linear.) dV/dI measurements were carried out by applying a dc current bias I_{dc} and a small ac current excitation (~13 Hz) through the sample ($I_{ac} = 1$ μA at $T > 1$ K and $I_{ac} = 10$ nA at $T < 1$ K), while measuring the ac voltage across the sample for 150 s and recording the average value for each I_{dc}.

Several cryostats were used to cover a wide range of temperatures and fields: a HelioxVL ^{3}He system ($0.25 \leqslant T \leqslant 200$ K) with H up to 9 T; a dilution refrigerator ($0.02 \leqslant T \lesssim 1$ K) and a ^{3}He system ($0.3 \leqslant T < 60$ K) in superconducting magnets with H up to 18 T; and a variable-temperature insert ($1.8 < T \leqslant 200$ K) in a Quantum Design PPMS with H up to 9 T. The fields, applied perpendicular to the film surface, were swept at constant temperatures. A low sweep rate of 0.1 T/min was used to avoid heating of the sample due to eddy currents. Measurements in the dilution refrigerator and the HelioxVL ^{3}He system were equipped with filters, consisting of a 1 kΩ resistor in series with a π-filter [5 dB (60 dB) EMI reduction at 10 MHz (1 GHz)] in each wire at the room temperature end of the cryostat to reduce high-frequency noise and heating by radiation. Furthermore, the dilution refrigerator and the ^{3}He system measurements in 18 T magnets were carried out in the Millikelvin Facility of the National High
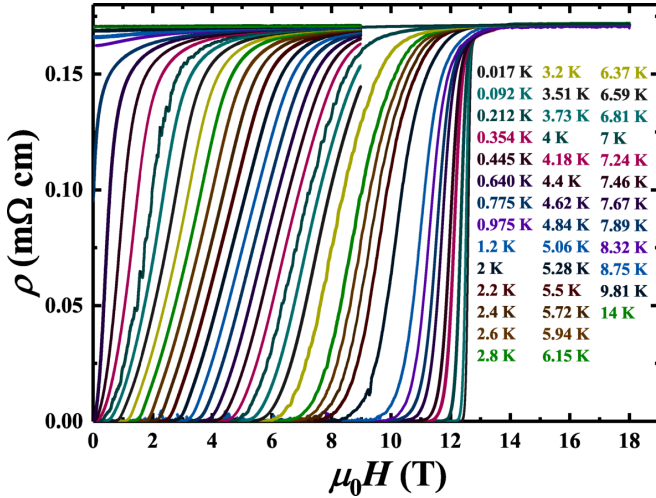
FIG. 4. Resistivity of a 22-nm-thick *a*-MoGe film at different *T*, ranging from 0.017 to 14 K, as a function of *H*. The data are shown for sample 1.

Magnetic Field Laboratory, which is an electromagnetically shielded room.

The resistivity curves obtained as a function of the applied magnetic field for different temperatures are shown in Fig. 4. The same curves are shown as a function of the temperature at different fields in Fig. 5(a). Figure 5(b) shows the resulting *T*-*H* phase diagram, shown on a linear scale in Fig. 2, on a log-*T* scale.

APPENDIX C: FITTING PROCEDURES

The *T*-dependence of the resistivity ρ at various fixed *H* was fitted to the Arrhenius and VFT forms: $\rho_{\mathrm{Arrh}} = \rho_0 \exp(-\frac{U(H)}{T})$ and $\rho_{\mathrm{VFT}} = \tilde{Z} \exp(-\frac{\tilde{W}(H)}{T - \tilde{T}_0(H)})$, respectively, as

described in the main text. We find that, at low *H*, ρ_{VFT} provides a better description of the data than ρ_{Arrh}. This is illustrated in Fig. 1(b). Here we present also examples for two more fields (3 and 8.2 T) for which the VFT and the Arrhenius fits were performed (Fig. 6). The low-field, *H* = 3 T resistivity data within the two red arrows follow the VFT fit (blue dotted line), and the data are pretty far from the Arrhenius fit (red dashed line). The high-field, *H* = 8.2 T resistivity data still follow the VFT fit better, but the deviation from the Arrhenius fit is getting smaller.

To compare with the results of numerical simulations, we also performed fits to the diffusion coefficient, D_v, using $\rho(T) = (h/2e)^2 n_{\mathrm{v}} D_{\mathrm{v}}/(k_B T)$, where $n_{\mathrm{v}} = B/\Phi_0$ is the vortex density and $D_{\mathrm{v}} = Z \exp(-\frac{W(H)}{T - T_0(H)})$. For both this fit and ρ_{VFT}, we implemented MATHEMATICA's global minimization feature to obtain the fitting parameters. In both cases, the fitting parameters were found to be the same within error, consistent with the exponential term dominating $\rho(T)$. The results for $T_0(H)$ obtained using fits to the diffusion coefficient are shown in Fig. 5(b), along with the values of $T_{\mathrm{c}}(H)$ and $H_{c2}(T)$ (see also Fig. 2 in the main text). We note that, when comparing the fits, we paid attention not only to the quality of the fit, but also to the range of temperatures where either one was effective—those ranges are shown in Fig. 2 of the main text.

Figure 7 shows all the parameters obtained from fits to the diffusion coefficient.

In Fig. 8, we compare the parameter *W* from fits to the diffusion coefficient with the parameter *U* from the ρ_{Arrh} fit for different values of *H*. For $H \gtrsim 9$ T where $T_0 = 0$, the two parameters are equal within error (Fig. 8), thus confirming the consistency of the analysis.

At these fields, the resistance *R* (or ρ) exhibits an orders-of-magnitude drop with decreasing *T*, and thus it can be fitted well with the Arrhenius form, as shown in Fig. 9(a). The parameters obtained from such ρ_{Arrh} fits for various fields
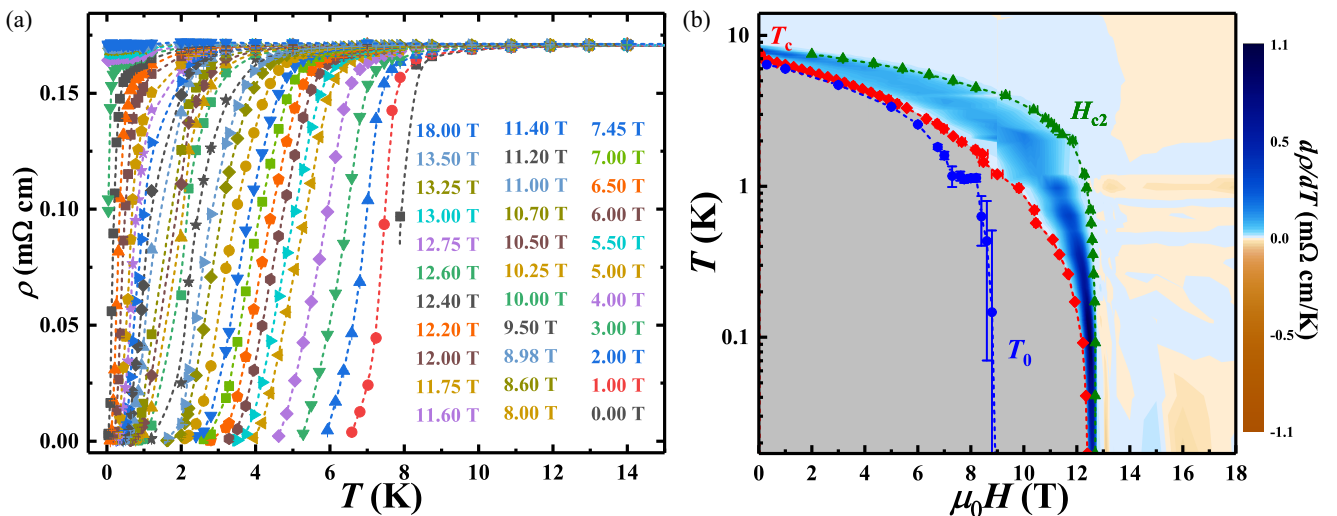

FIG. 5. Resistivity and the (*T*, *H*) phase diagram of a 22-nm-thick *a*-MoGe film. The data are shown for sample 1. (a) $\rho(T)$ at different *H* over a range of temperatures ($0.017 \leqslant T \leqslant 14$ K), shown on a linear scale. Dashed lines guide the eye. (b) *T*-*H* phase diagram in a log-*T* scale: T_{c} (red diamonds), H_{c2} (green triangles), and T_0 (blue dots) represent the superconducting transition temperature, dependent on our experimental resolution, the upper critical field, and the transition to a vortex solid, respectively. The error bars in T_0 reflect the standard error from the VFT fits; error bars in $T_{\mathrm{c}}(H)$ and H_{c2} represent the uncertainty in defining the magnetic field where resistance rises above the noise floor or reaches 95% of the normal state resistance, respectively. The color map corresponds to $d\rho/dT$.
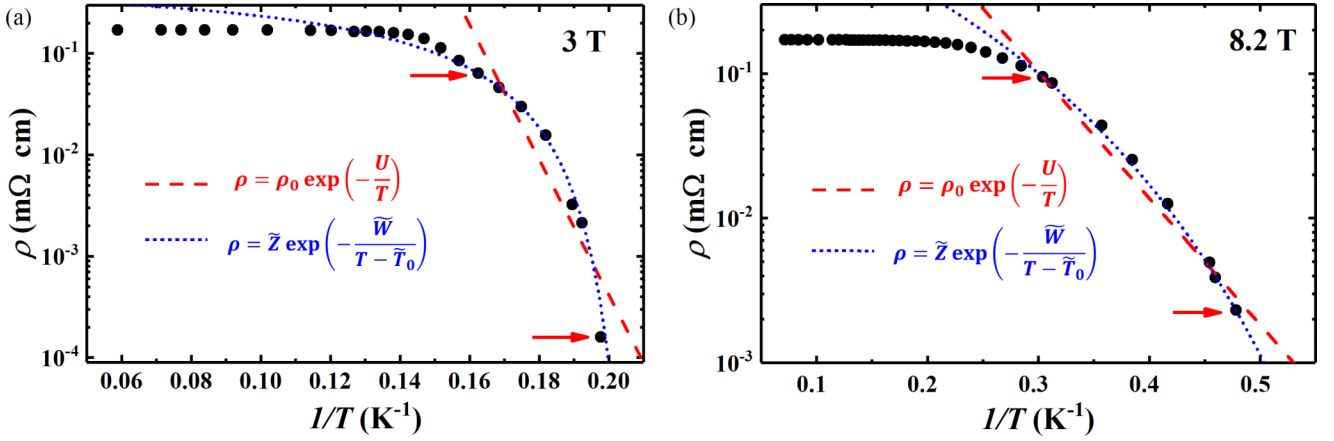
FIG. 6. Comparison of the Arrhenius and VFT fits of $\rho(T)$. The data are shown for sample 1; $I_{exc} = 100$ nA. (a) $H = 3$ T; $\tilde{T}_0 = (4.71 \pm 0.02)$ K. (b) $H = 8.2$ T; $\tilde{T}_0 = (1.25 \pm 0.06)$ K. In both panels, the Arrhenius (red dashed lines) and VFT (blue dotted lines) fits are performed to the data shown within the two red arrows. The VFT form describes the data better, especially at the lowest T. Since $\tilde{T}_0$ decreases with increasing H, the difference between the two fits also decreases at higher fields. For the same data, fits to the diffusion coefficient [Eq. (2) in the main text] yield $T_0 = (4.69 \pm 0.02)$ and (1.14 ± 0.06) K for 3 and 8.2 T, respectively; these values are the same within error as the corresponding $\tilde{T}_0$.

are shown in Fig. 9(b). The activation energy U shows a logarithmic dependence on H as expected from the TAFF model and the logarithmic vortex-vortex interaction in 2D [20].

APPENDIX D: NONLINEAR TRANSPORT

We find that the V-I characteristic at low enough T remains non-Ohmic (i.e., nonlinear) for $I_{dc} \neq 0$, and dV/dI increases with I_{dc} [Figs. 10(a) and 10(b)]. Such nonlinear transport is expected from the motion of vortices in the presence of disorder, i.e., it is a signature of a viscous vortex liquid [23]. As T increases, nonlinear behavior is no longer observed

[Figs. 10(c) and 10(d)]. At $T < T_c$, where ρ drops below our noise floor, a finite I_{dc} (i.e., a critical current) is then needed to depin a measurable number of vortices [Fig. 10(e)]. Since $\rho(T)$ in the liquid phase at high fields can only be fitted with the Arrhenius law $\rho_{Arrh} = \rho_0 \exp(-\frac{U(H)}{T})$, our transport results suggest that in this regime an isotropic vortex liquid freezes into an amorphous vortex glass as $T \to 0$, i.e., the solid phase is only realized at $T = 0$.

In the normal state ($H > H_{c2}$), V-I characteristics are Ohmic, i.e., we find a linear response [Figs. 10(b) and 10(e)], as expected. In the low-H ($H < H^*$, $T_0 \neq 0$, $T > T_c$) regime ("VFT" in Fig. 2 of the main text), we also find Ohmic
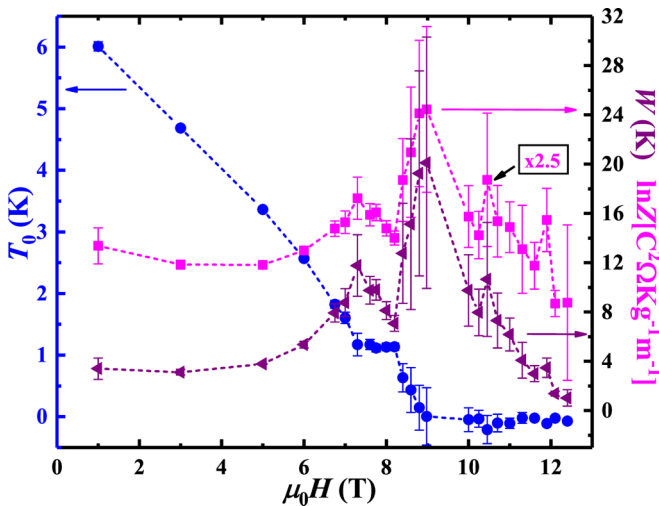

FIG. 7. The VFT fitting parameters T_0, W, and $\ln Z$. The data are shown for sample 1. The error bars represent standard errors obtained from the nonlinear fits of $(\frac{2e}{\hbar})^2 k_B \rho T$ to the VFT law in Eq. (2) of the main text. A strong correlation between W (purple triangles) and $\ln Z$ (magenta squares) is observed ($\ln Z$ is multiplied by 2.5 on the y-axis for clarity). T_0 (blue dots) is independent of the other two parameters.
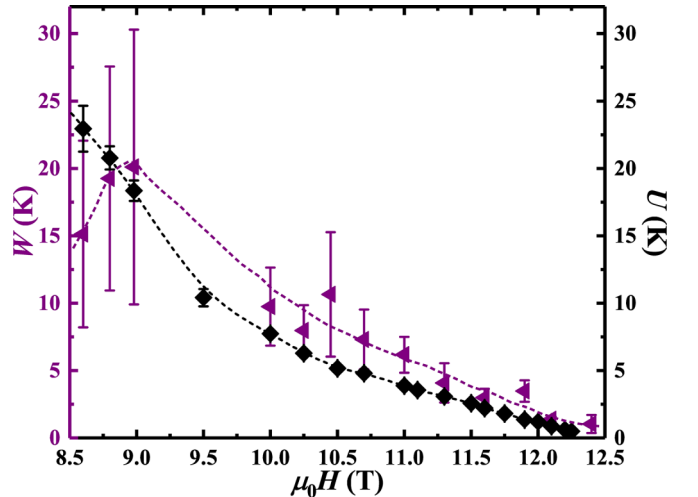

FIG. 8. Comparison of the parameters W (from the VFT fit) and U (from the Arrhenius fit). The data are shown for sample 1. W (purple triangles) and U (black diamonds) are equal, within error, for $H \gtrsim 9$ T where $T_0 = 0$, thus confirming the consistency of the analysis. Dashed lines guide the eye. The error bars for W and U are standard errors from the nonlinear fit of $(\frac{2e}{\hbar})^2 k_B \rho T$ to the VFT form and the linearized fit of ρ to the Arrhenius form, respectively.

(a)

(b)

$$R = R_0 \exp\left(-\frac{U}{T}\right)$$

12.25 T
12.20 T
12.10 T
12.00 T
11.90 T
11.75 T
11.60 T
11.50 T
11.30 T
11.10 T
11.00 T
10.90 T
10.70 T
10.50 T
10.25 T
10.00 T

$$U(H) = U_0 \ln\left(\frac{H_0}{H}\right)$$

$$U_0 = 31.5 \pm 0.4 \text{ K}$$
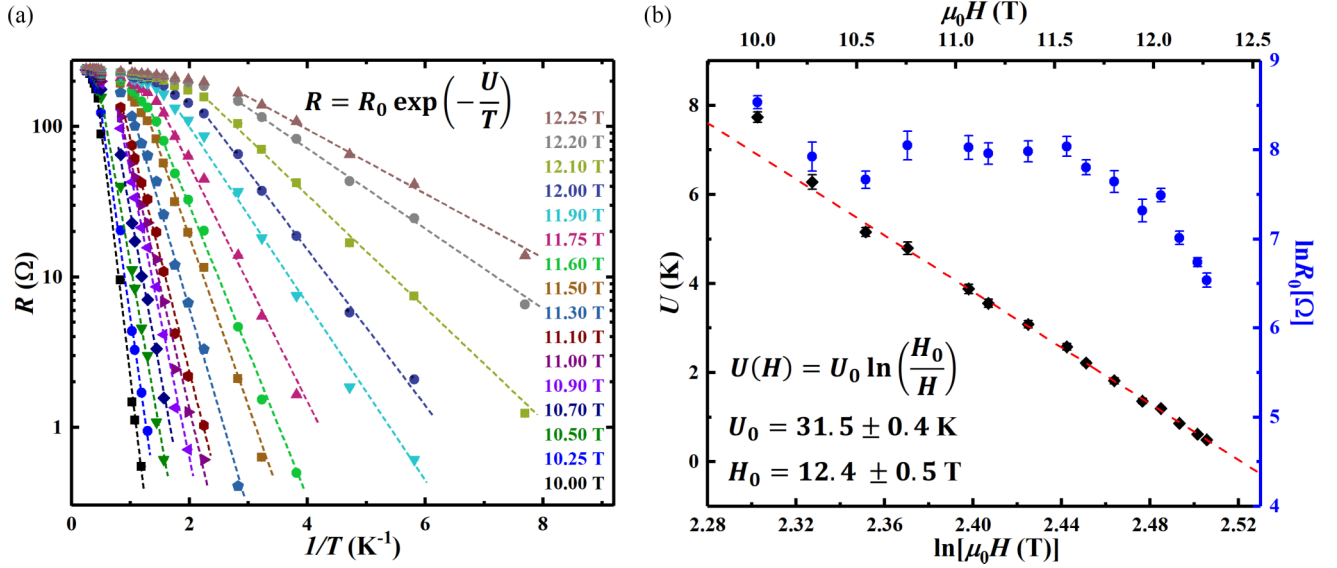
$$H_0 = 12.4 \pm 0.5 \text{ T}$$

FIG. 9. Arrhenius $R(T)$ in the high-field ($T_0 = 0$) regime. The data are shown for sample 1. (a) Resistance R vs $1/T$ for fixed fields. Dashed lines are linear least-squares fits. (b) The fitting parameters from (a), i.e., activation energy U (black diamonds) and $\ln R_0$ (blue dots), vs H. The error bars represent standard errors obtained from the linearized fits in (a). $U(H) = U_0 \ln(H_0/H)$, where $U_0 = (31.5 \pm 0.4)$ K and $H_0 = (12.4 \pm 0.5)$ T. The red dashed line is a linear least-squares fit.

behavior [Fig. 10(f)]. However, since this regime is measured only at relatively high T, in analogy with the Arrhenius region we speculate that any nonlinear transport that might be present for small I_{dc} at lower T is experimentally inaccessible.

APPENDIX E: MONTE CARLO SIMULATIONS

We have performed Monte Carlo (MC) simulations on a spin system on a square grid with lattice spacing $a = 1$, linear size $L = 56$, and uniform magnetic field, whose intensity can be expressed in terms of the quantum-flux fraction f passing through a unitary plaquette $f = Ba^2/\Phi_0$. Here we considered $f = 1/L$, which results in $N_v = fL^2 = 56$ vortices with a given vorticity. Although the system size simulated is smaller than in other numerical simulations of particle systems [10,34–37,39], it is the state of the art for numerical simulations of vortex lattices within XY models. Each MC step consists of the local updating of all spins of the lattice by means of the Metropolis-Hastings algorithm. All observables have been computed at equilibrium, as achieved after a certain number $\bar{t}$ of MC steps. For temperatures above T_0, we identify $\bar{t}$ with the entrance into the diffusive regime, while below T_0 we estimated that $\bar{t} \simeq 10^8$ MC steps provides a stable result. After discarding the first $\bar{t}$ steps, we reset the Monte Carlo time and proceed with the measurements of both the statical and the dynamical observables.

The superfluid stiffness J_s is defined as the linear response to an infinitesimal phase twist in a given direction, say μ, and it reads

$$J_s^\mu = J_d^\mu - J_p^\mu, \tag{E1}$$

$$J_d^\mu = \frac{J}{L^2}\left\langle \sum_i \cos\left(\theta_i - \theta_{i+\mu} + F_i^\mu\right)\right\rangle, \tag{E2}$$

$$J_p^\mu = \frac{J^2}{TL^2}\left\langle\left[\sum_i \sin\left(\theta_i - \theta_{i+\mu} + F_i^\mu\right)\right]^2\right\rangle$$
$$- \frac{J^2}{TL^2}\left\langle\sum_i \sin\left(\theta_i - \theta_{i+\mu} + F_i^\mu\right)\right\rangle^2. \tag{E3}$$

It accounts for two contributions: the diamagnetic part J_d^μ, proportional to the energy density of the system, and the paramagnetic part J_p^μ, given by the connected current-current response function. Here and in what follows, $\langle \cdots \rangle$ stands for both the thermal average, performed at equilibrium over all the MC steps, and the average over 10 independent numerical simulations.

The local orientational order parameter ψ_{6j} is obtained by means of a Delaunay triangulation of the VL. It is defined for hexagonal symmetry as

$$\psi_{6j} = \frac{1}{N_j}\sum_{k=1}^{N_j} e^{6i\theta_{jk}}, \tag{E4}$$

where N_j is the number of nearest neighbors of the jth vortex, and θ_{jk} is the angle that the bond connecting the two neighboring vortices j and k forms with respect to a fixed direction in the plane. The global sixfold orientational order parameter G_6 is then obtained by summing over all the N_v vortices and by computing its average, i.e., $G_6 = \langle\frac{1}{N_v}\sum_{j=1}^N \psi_{6j}\rangle$. The susceptibility of the orientational order parameter χ_6 is defined as

$$\chi_6 = \left\langle\Psi_6^2\right\rangle - \langle\Psi_6\rangle^2, \tag{E5}$$

where $\Psi_6 = \frac{1}{N_v}\sum_{j=1}^{N_v} \psi_{6j}$, with ψ_{6j} defined in (E4). The temperature dependence of χ_6 (Fig. 11) exhibits a peak at $T = 0.05$ that we identify as the critical temperature T_{hex} between the hexatic and the isotropic liquid phase.
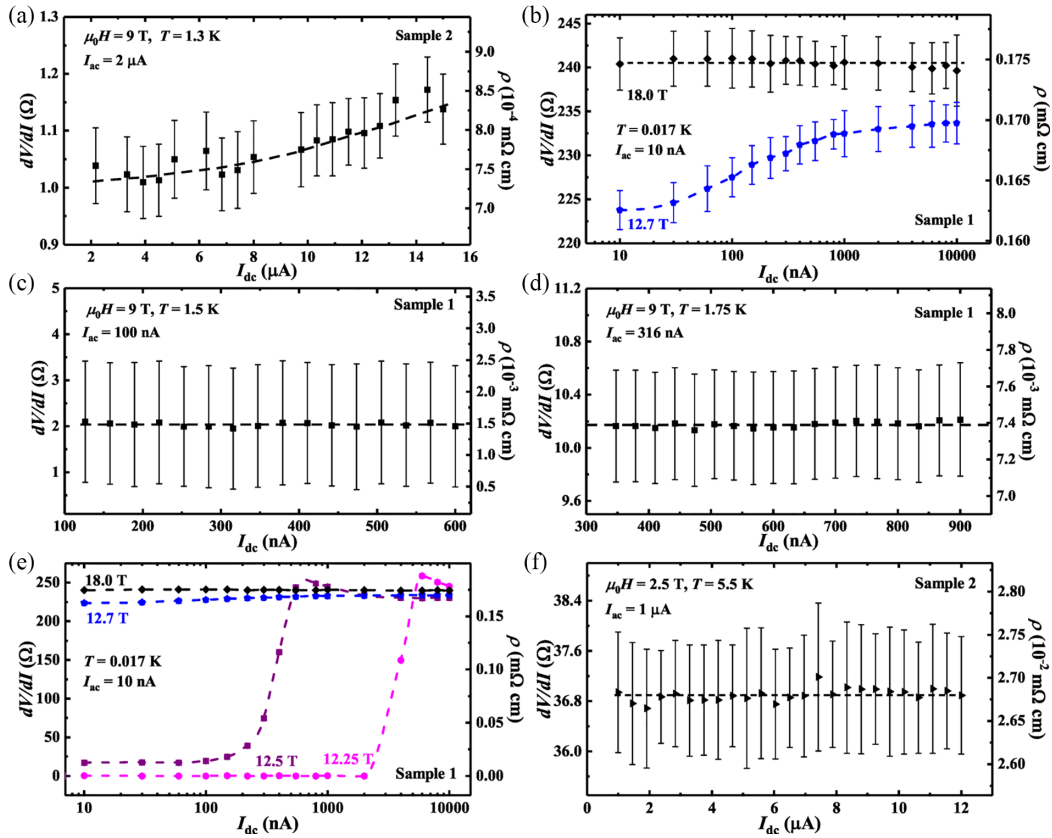
FIG. 10. Differential resistance dV/dI as a function of dc current I_{dc} in different regimes. (a) In the "Arrhenius" region (Fig. 2) at $T = 1.3$ K and $H = 9$ T, a strong nonlinearity is observed, consistent with the motion of vortices in the presence of disorder; $T_c(H = 9$ T$) = 1.1 \pm 0.2$ K. (b) Similar nonlinear dV/dI vs I_{dc} in the "Arrhenius" region for $H = 12.7$ T and $T = 0.017$ K. At a much higher field ($H = 18.0$ T $> H_{c2}$), in the normal state, dV/dI vs I_{dc} is Ohmic. The nonlinear behavior becomes unobservable also as T increases, as shown in (c), for $H = 9$ T at $T = 1.5$ K, and (d), for $H = 9$ T at $T = 1.75$ K, at lower currents than in (a). (e) The evolution of dV/dI vs I_{dc} with increasing H, as shown, at $T = 0.017$ K. The data for $H = 18.0$ and 12.7 T are the same as in (b). When ρ drops below the noise floor, e.g., for $H = 12.25$ T, a finite $I_{dc} \simeq 2$ μA, i.e., a critical current, is needed to depin a measurable number of vortices. At somewhat higher $H = 12.5$ T, ρ is nonzero at low current bias, consistent with the vortex creep due to thermal fluctuations. The depinning effect becomes observable at the critical current $I_{dc} \sim 0.1$ μA, which is lower than that for $H = 12.25$ T, as expected. (f) dV/dI vs I_{dc} is Ohmic at $T \approx 5.5$ K and $H = 2.5$ T, where $\rho(T)$ obeys the VFT law. At this field, $T_0 \approx 5$ K and $T_c \approx 5.37$ K (Fig. 2). The error bars in all panels correspond to ± 1 SD obtained from averaging the ac voltage over 150 s at a fixed I_{dc}. Dashed lines guide the eye. The T fluctuations for these measurements were less than 5 mK.

Due to the small size of our system, we cannot discriminate between a floating solid [29,33] and a hexatic liquid based on the static properties. Nonetheless, the dynamic features of the vortices show all the typical fingerprints of the hexatic phase, as they have been identified in 2D soft-colloidal systems [35–39].

1. Monte Carlo simulations: Static characterization of the vortex lattice

To further characterize the three phases found, we have computed the structure factor of the vortex lattice defined as

$$S(\mathbf{k}) = \frac{1}{2N_v^2} \sum_{i,j} \exp[i\mathbf{k} \cdot (\mathbf{r_i} - \mathbf{r_j})]\langle \nu(\mathbf{r_i})\nu(\mathbf{r_j})\rangle, \quad \text{(E6)}$$

where N_v is the total number of vortices, $\nu(\mathbf{r_i})$ is the local vortex density, equal to 1 if a vortex occupies the site $\mathbf{r_i}$ and zero otherwise, and $\mathbf{k}$ is the vortex lattice reciprocal vector. In Fig. 12, we show $S(\mathbf{k})$ computed at three different temperatures: $T = 0.02, 0.04, 0.07$, corresponding, respectively, to

the solid, hexatic-liquid, and isotropic-liquid phase. At high T, the structure factor presents the typical circular symmetry of an isotropic liquid. Decreasing the T, such symmetry breaks down and the Bragg-peaks structure appears showing six well-defined spots. Finally, in the solid state the Bragg peaks become well-defined even at large k. Let us highlight that the structure-factor anisotropy observed at low T is due to the commensurability of the VL with respect to the underlying square lattice of spins. The VL has indeed two ways to align with respect to the underlying square lattice: to be perfectly commensurate with either the $\hat{x}$-axis or the $\hat{y}$-axis.

To identify the isotropic to hexatic liquid transition, we have computed the orientational susceptibility χ_6. The susceptibility of the orientational order parameter χ_6 is defined as

$$\chi_6 = \langle \Psi_6^2 \rangle - \langle \Psi_6 \rangle^2, \quad \text{(E7)}$$

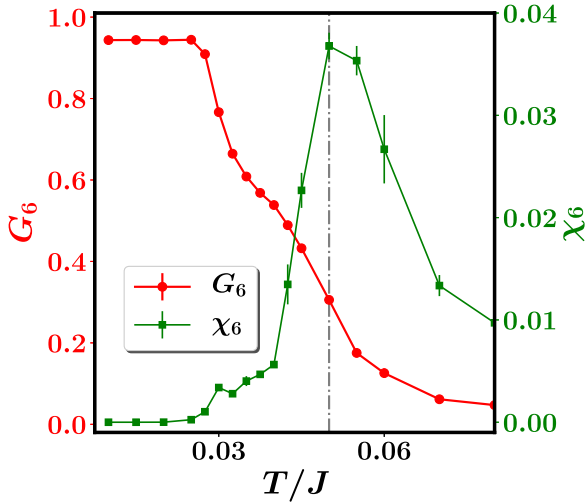where $\Psi_6 = \frac{1}{N_v} \sum_{j=1}^{N_v} \psi_{6j}$ with ψ_{6j} defined in Eq. (E4) above.

FIG. 11. Orientational order parameter and susceptibility. Orientational order parameter G_6 and the corresponding orientational susceptibility χ_6 as a function of the temperature in units of the coupling constant of the XY model J. The peak of the orientational susceptibility identifies the temperature T_{hex} separating the hexatic from the isotropic liquid phase.

2. Monte Carlo simulations: Signatures of heterogeneous dynamics

The heterogeneous nature of the vortex dynamics in the hexatic phase has its fingerprints in different observables. Together with the mean-square displacement $\langle \Delta r^2(t) \rangle$, discussed in the main text, we also computed the self-part of the intermediate scattering function $F_s(|\mathbf{k}^*|, t)$, and the non-Gaussian parameter $\alpha_2(t)$. The resulting trends in time for different temperatures are shown in Fig. 13, where the time variable t labels the discrete MC steps. To highlight the onset of the hexatic phase, the curves at the verge of the isotropic-liquid to the hexatic-liquid transition ($T = 0.05$) have been plotted in gray.

The self-part of the intermediate scattering function is a dynamical autocorrelation function for the VL, and it is defined as

$$F_s(|\mathbf{k}^*|, t) = \frac{1}{N_v} \sum_{j=1}^{N_v} \frac{1}{(t_M - t)} \sum_{t_0=0}^{t_M - t} \frac{1}{N_{\mathbf{k}}}$$
$$\times \sum_{\mathbf{k}:|\mathbf{k}|=|\mathbf{k}^*|} \overline{\exp\{i\mathbf{k}[\mathbf{r}_j(t_0 + t) - \mathbf{r}_j(t_0)]\}}, \quad \text{(E8)}$$

where $|\mathbf{k}^*| = 2\pi/a_v$ (with a_v the lattice spacing of the VL) is the reciprocal vector at which the structure factor shows its first peak (see Fig. 12), $\mathbf{r}_j(t)$ is the position of the jth vortex at the MC time t, and t_M is the largest MC time used in the simulations. The thermal average is thus the sum over all the possible t_0 for a given time t, while $\overline{(\cdots)}$ stands for the average over 10 independent simulations. From Fig. 13(a), one can see that, in the isotropic liquid phase, $F_s(|\mathbf{k}_{\text{max}}|, t)$ decays exponentially to zero with a unique relaxation time. On the other hand, as the hexatic phase is approached, it starts showing a plateau, which increases with decreasing T. This two-step relaxation decay is another typical signature of a
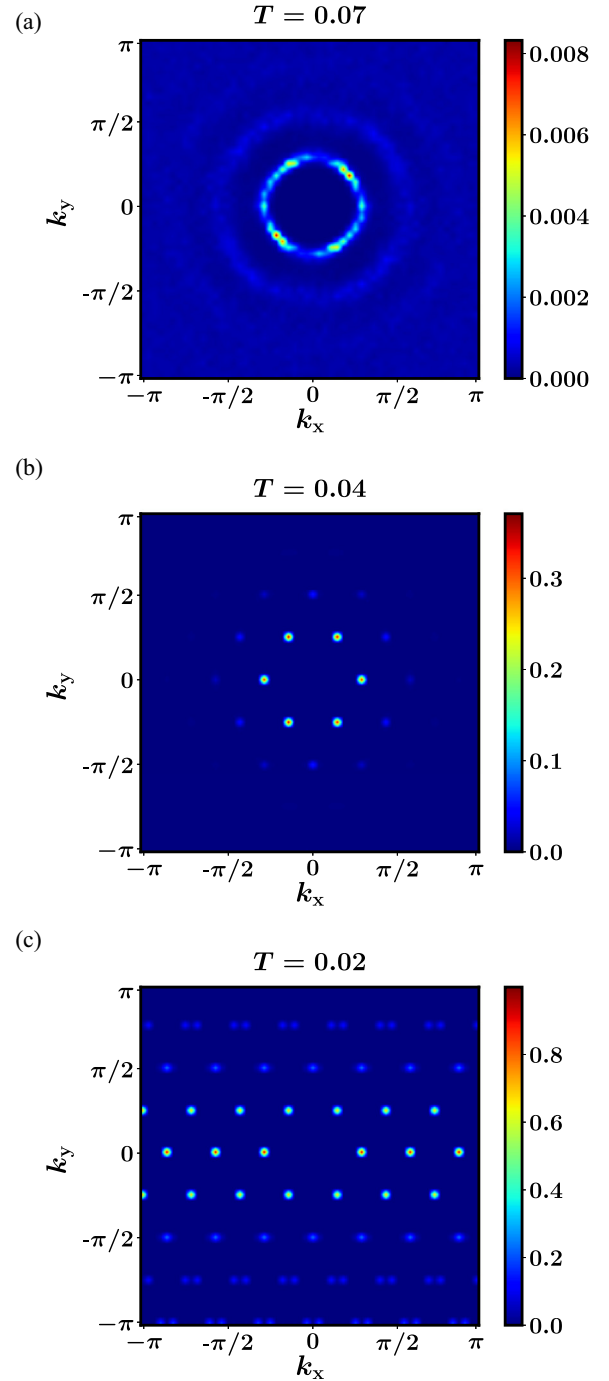

FIG. 12. Structure factor of the vortex lattice in the three phases. Structure factor computed for a given sample at three different temperatures corresponding to the three different phases: $T = 0.07$ isotropic liquid phase; $T = 0.04$ hexatic liquid phase; $T = 0.02$ solid phase. To highlight the main features of the structure factor, we have fixed $S(\mathbf{k} = 0) = 0$.

caging mechanism [15] due in this case to the onset of the hexatic phase. The mean-square displacement, already shown in the inset of Fig. 3(b) and in Fig. 13(b), is defined as

$$\langle \Delta r^2(t) \rangle = \frac{1}{N_v} \sum_{j=1}^{N_v} \frac{1}{(t_M - t)} \sum_{t_0=0}^{t_M - t} \overline{|\mathbf{r}_j(t_0 + t) - \mathbf{r}_j(t_0)|^2}. \quad \text{(E9)}$$
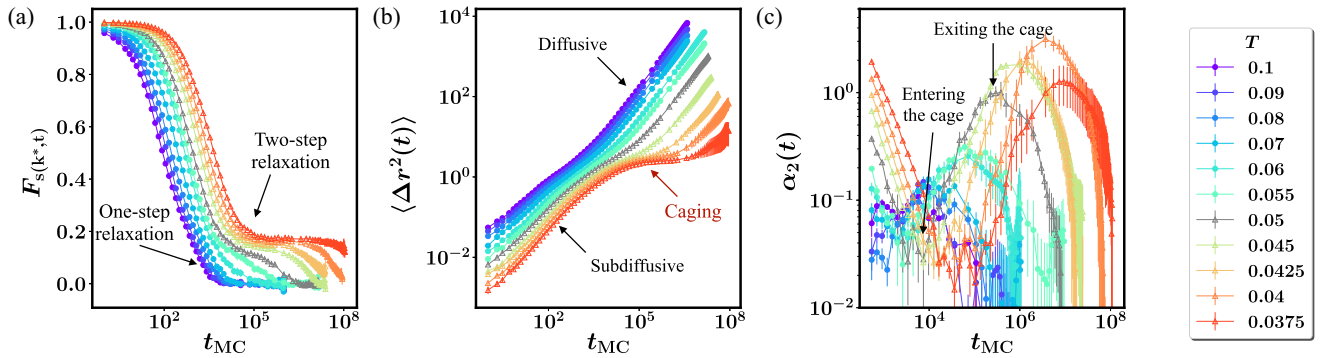
FIG. 13. Dynamic characteristics of the liquid phase. (a) The self-part of the intermediate scattering function computed at $|\mathbf{k}^*| = 2\pi/a_v$, with a_v the lattice spacing of the VL; (b) the mean-square displacement; and (c) the non-Gaussian parameter as a function of the MC time for different temperatures. The two arrows, which indicate entry into and exit from the cage, refer to the temperature $T = 0.05$ plotted in gray. In all panels, gray lines correspond to the hexatic critical temperature $T_{hex} = 0.05$.

As briefly introduced in the main text, $\langle \Delta r^2(t) \rangle$ is computed for each individual vortex at several T. At high T, $\langle \Delta r^2(t) \rangle$ directly crosses over from the short-time subdiffusive regime (due to the presence of the numerical square grid) to the typical long-time diffusive behavior, where $\langle \Delta r^2(t) \rangle \sim D_v t$, with D_v the vortex diffusion constant. However, at the verge of the isotropic- to hexatic-liquid transition, an additional subdiffusive regime appears with a strong suppression of $\langle \Delta r^2(t) \rangle$ [see Fig. 13(b) and Fig. 3(b), inset] at intermediate timescales that is the hallmark of dynamical heterogeneities (see also Video S1 in the Supplemental Material [40]). This signals an inhibition of the particle motion due to the cage formed by the neighboring particles, similar to what happens in supercooled liquid and glassy systems. The signatures of the dynamical heterogeneities persist at longer timescales, with a marked reduction at these temperatures of the asymptotic diffusion coefficient, defined as $D_v = \frac{1}{4} \lim_{t \to \infty} \langle \Delta r^2(t) \rangle / t$.

The intermediate plateau observed both in the mean-square displacement and in the intermediate scattering function signals the emergence of a heterogeneous dynamics within a certain timescale. To further investigate this behavior, we have computed the non-Gaussian parameter

$$\alpha_2(t) = \frac{1}{2} \frac{\langle \Delta \mathbf{r}^4(t) \rangle}{\langle \Delta \mathbf{r}^2(t) \rangle^2} - 1, \qquad (E10)$$

which quantifies the heterogeneity of the dynamics in terms of strength and extent in time [46]. We find [Fig. 13(c)] that, at very short times, the VL displays a strongly heterogeneous dynamics for all the temperatures analyzed. This anomalous behavior is due to the underlying squared grid of spins that forces vortices to move only along four possible directions: $\pm \hat{x}$ and $\pm \hat{y}$. With increasing time, the direction of motion becomes less sensitive to the underlying grid, and $\alpha_2(t)$ decreases. Apart from the initial heterogeneity, at high temperatures the VL shows a homogeneous dynamics. On the

other hand, at the onset of the hexatic phase, the non-Gaussian parameter starts displaying a dome at longer timescales. This additional signature of heterogeneity is another indication of a caging mechanism triggered by the onset of the hexatic phase. With decreasing T, the height of the dome increases, signaling the increase of the heterogeneous dynamics strength. At the same time, the peak of the dome moves to longer times, reflecting the increase of the timescale at which vortices escape from their cage.

APPENDIX F: BRIEF DESCRIPTION OF THE SUPPLEMENTAL VIDEO

Supplemental Video S1: Heterogeneous vortex motion in the hexatic phase [40]. Images of the vortex motion at $T = 0.045$ for different MC times. In this regime, the dynamics is strongly heterogeneous in both space and time. The vortices remain indeed trapped for a long time in the cage formed by their neighbors before exiting in a collective burst along the symmetry axis of the vortex lattice.

In the video, the vortices are represented as colored disks, centered at a given position $\mathbf{x_i}$ at time t_i. Each frame shows vortex evolution over 10 consecutive discrete time steps t_i. To help visualize the time evolution, we assigned to each disk a radius r_i that is increasing with increasing time t_i. As a consequence, larger disks identify the vortex position at larger times. In addition, we add a solid black line connecting the centers of the disks to help visualize the vortex motion as a function of time. The gray lines in the background show the trails left by the vortices during the whole simulation. The horizontal line at the bottom of the image indicates the time flow. Note that the time steps t_i are not equally spaced with respect to the MC time. Indeed, for the sake of the memory allocation, we have stored the data each $t_{MC} = \text{int}(A^q) + kA^{N_q}$, with $q \in [0, N_q]$, $k \in [0, N_k]$, and $A = 1.3$.

[1] J. M. Kosterlitz, Kosterlitz–Thouless physics: A review of key issues, Rep. Prog. Phys. **79**, 026001 (2016).

[2] V. N. Ryzhov, E. E. Tareyeva, Y. D. Fomin, and E. N. Tsiok, Berezinskii–Kosterlitz–Thouless transition and two-dimensional melting, Phys.-Usp. **60**, 857 (2017).

[3] B. I. Halperin and D. R. Nelson, Theory of Two-Dimensional Melting, Phys. Rev. Lett. **41**, 121 (1978).

[4] D. R. Nelson and B. I. Halperin, Dislocation-mediated melting in two dimensions, Phys. Rev. B **19**, 2457 (1979).

[5] A. P. Young, Melting and the vector Coulomb gas in two dimensions, Phys. Rev. B **19**, 1855 (1979).

[6] I. Guillamón, H. Suderow, A. Fernández-Pacheco, J. Sesé, R. Córdoba, J. De Teresa, M. Ibarra, and S. Vieira, Direct observation of melting in a two-dimensional superconducting vortex lattice, Nat. Phys. **5**, 651 (2009).

[7] I. Guillamón, R. Córdoba, J. Sesé, J. M. De Teresa, M. R. Ibarra, S. Vieira, and H. Suderow, Enhancement of long-range correlations in a 2D vortex lattice by an incommensurate 1D disorder potential, Nat. Phys. **10**, 851 (2014).

[8] I. Roy, S. Dutta, A. N. R. Choudhury, S. Basistha, I. Maccari, S. Mandal, J. Jesudasan, V. Bagwe, C. Castellani, L. Benfatto, and P. Raychaudhuri, Melting of the Vortex Lattice through Intermediate Hexatic Fluid in an *a*-MoGe Thin Film, Phys. Rev. Lett. **122**, 047001 (2019).

[9] S. Dutta, I. Roy, S. Mandal, J. Jesudasan, V. Bagwe, and P. Raychaudhuri, Extreme sensitivity of the vortex state in *a*-MoGe films to radio-frequency electromagnetic perturbation, Phys. Rev. B **100**, 214518 (2019).

[10] M. Chandran, R. T. Scalettar, and G. T. Zimányi, Domain regime in two-dimensional disordered vortex matter, Phys. Rev. B **69**, 024526 (2004).

[11] E. Dagotto, Complexity in strongly correlated electronic systems, Science **309**, 257 (2005).

[12] H. Vogel, The temperature dependence law of the viscosity of fluids, Phys. Z. **22**, 645 (1921).

[13] G. S. Fulcher, Analysis of recent measurements of the viscosity of glasses, J. Am. Ceram. Soc. **8**, 339 (1925).

[14] G. Tammann and W. Hesse, The dependence of the viscosity on the temperature in supercooled liquids, Z. Anorg. Allg. Chem. **156**, 245 (1926).

[15] A. Cavagna, Supercooled liquids for pedestrians, Phys. Rep. **476**, 51 (2009).

[16] J. M. Graybeal and M. R. Beasley, Localization and interaction effects in ultrathin amorphous superconducting films, Phys. Rev. B **29**, 4167 (1984).

[17] S. Dutta, I. Roy, S. Basistha, S. Mandal, J. Jesudasan, V. Bagwe, and P. Raychaudhuri, Collective flux pinning in hexatic vortex fluid in *a*-MoGe thin film, J. Phys.: Condens. Matter **32**, 075601 (2020).

[18] A. Yazdani, C. M. Howald, W. R. White, M. R. Beasley, and A. Kapitulnik, Competition between pinning and melting in the two-dimensional vortex lattice, Phys. Rev. B **50**, 16117 (1994).

[19] B. Plourde, D. Van Harlingen, D. Vodolazov, R. Besseling, M. Hesselberth, and P. Kes, Influence of edge barriers on vortex dynamics in thin weak-pinning superconducting strips, Phys. Rev. B **64**, 014503 (2001).

[20] G. Blatter, M. V. Feigel'man, V. B. Geshkenbein, A. I. Larkin, and V. M. Vinokur, Vortices in high-temperature superconductors, Rev. Mod. Phys. **66**, 1125 (1994).

[21] D. Ephron, A. Yazdani, A. Kapitulnik, and M. R. Beasley, Observation of Quantum Dissipation in the Vortex State of a Highly Disordered Superconducting Thin Film, Phys. Rev. Lett. **76**, 1529 (1996).

[22] K. Ienaga, T. Hayashi, Y. Tamoto, S. Kaneko, and S. Okuma, Quantum Criticality inside the Anomalous Metallic State of a Disordered Superconducting Thin Film, Phys. Rev. Lett. **125**, 257001 (2020).

[23] T. Giamarchi, Disordered elastic media, in *Encyclopedia of Complexity and Systems Science*, edited by R. A. Meyers (Springer, New York, 2009), pp. 2019–2038.

[24] M. Giura, R. Marcon, E. Silva, and R. Fastampa, Magnetic dissipation in high-T_c superconductors: Evidence for a vortex-glass-to-vortex-liquid transition, Phys. Rev. B **46**, 5753 (1992).

[25] C. Reichhardt, A. van Otterlo, and G. T. Zimányi, Vortices Freeze like Window Glass: The Vortex Molasses Scenario, Phys. Rev. Lett. **84**, 1994 (2000).

[26] Y. Kato and N. Nagaosa, Monte Carlo simulation of two-dimensional flux-line-lattice melting, Phys. Rev. B **48**, 7383 (1993).

[27] R. Šášik and D. Stroud, Calculation of the shear modulus of a two-dimensional vortex lattice, Phys. Rev. B **49**, 16074 (1994).

[28] T. Saiki and R. Ikeda, Vortex lattice melting in two-dimensional superconductors in intermediate fields, Phys. Rev. B **83**, 174501 (2011).

[29] S. A. Hattel and J. M. Wheatley, Flux-lattice melting and depinning in the weakly frustrated two-dimensional XY model, Phys. Rev. B **51**, 11951 (1995).

[30] A. Tanaka and X. Hu, Numerical study of the flux lattice melting transition in 2D superconductors, Physica C **357–360**, 438 (2001).

[31] I. Maccari, L. Benfatto, and C. Castellani, Uniformly frustrated XY model: Strengthening of the vortex lattice by intrinsic disorder, Condens. Matter **6**, 42 (2021).

[32] M. Franz and S. Teitel, Vortex Lattice Melting in 2D Superconductors and Josephson Arrays, Phys. Rev. Lett. **73**, 480 (1994).

[33] M. Franz and S. Teitel, Vortex-lattice melting in two-dimensional superconducting networks and films, Phys. Rev. B **51**, 6551 (1995).

[34] C. Reichhardt, C. J. Olson, R. T. Scalettar, and G. T. Zimányi, Commensurate and incommensurate vortex lattice melting in periodic pinning arrays, Phys. Rev. B **64**, 144509 (2001).

[35] R. Zangi and S. A. Rice, Cooperative Dynamics in Two Dimensions, Phys. Rev. Lett. **92**, 035502 (2004).

[36] J. Kim, C. Kim, and B. J. Sung, Simulation Study of Seemingly Fickian but Heterogeneous Dynamics of Two Dimensional Colloids, Phys. Rev. Lett. **110**, 047801 (2013).

[37] S. C. Kapfer and W. Krauth, Two-Dimensional Melting: From Liquid-Hexatic Coexistence to Continuous Transitions, Phys. Rev. Lett. **114**, 035702 (2015).

[38] A. L. Thorneywork, J. L. Abbott, D. G. A. L. Aarts, and R. P. A. Dullens, Two-Dimensional Melting of Colloidal Hard Spheres, Phys. Rev. Lett. **118**, 158001 (2017).

[39] B. van der Meer, W. Qi, J. Sprakel, L. Filion, and M. Dijkstra, Dynamical heterogeneities and defects in two-dimensional soft colloidal crystals, Soft Matter **11**, 9385 (2015).

[40] See Supplemental Material at http://link.aps.org/supplemental/10.1103/PhysRevB.107.014509 for a video of transport signatures of fragile glass dynamics in the melting of the two-dimensional vortex lattice.

[41] A. Yazdani, W. White, M. Hahn, M. Gabay, M. Beasley, and A. Kapitulnik, Observation of Kosterlitz-Thouless-type Melting of the Disordered Vortex Lattice in Thin Films of *a*-MoGe, Phys. Rev. Lett. **70**, 505 (1993).

[42] X. Shi, P. V. Lin, T. Sasagawa, V. Dobrosavljević, and D. Popović, Two-stage magnetic-field-tuned superconductor-insulator transition in underdoped $La_{2-x}Sr_xCuO_4$, Nat. Phys. **10**, 437 (2014).

[43] Z. Shi, P. G. Baity, T. Sasagawa, and D. Popović, Vortex phase diagram and the normal state of cuprates with charge and spin orders, Sci. Adv. **6**, eaay8946 (2020).

[44] B. Rosenstein and D. Li, Ginzburg-Landau theory of type II superconductors in magnetic field, Rev. Mod. Phys. **82**, 109 (2010).

[45] L. W. Bruch, R. D. Diehl, and J. A. Venables, Progress in the measurement and modeling of physisorbed layers, Rev. Mod. Phys. **79**, 1381 (2007).

[46] A. Rahman, Correlations in the motion of atoms in liquid argon, Phys. Rev. **136**, A405 (1964).